



The effect of chromium substitution on improving electrochemical performance of low-cost Fe–Mn based Li-rich layered oxide as cathode material for lithium-ion batteries



Taolin Zhao^a, Li Li^{a,*}, Shi Chen^a, Renjie Chen^a, Xiaoxiao Zhang^a, Jun Lu^b, Feng Wu^a, Khalil Amine^{b,1}

^aSchool of Chemical Engineering and the Environment, Beijing Key Laboratory of Environmental Science and Engineering, Beijing Institute of Technology, Beijing 100081, China

^bChemical Sciences and Engineering Division, Argonne National Laboratory, IL 60439, USA

HIGHLIGHTS

- We have prepared new cathode materials $\text{LiFe}_{1-x}\text{Cr}_x\text{O}_2 \cdot \text{Li}_2\text{MnO}_3$ ($x = 0, 0.1, 0.25, 0.5$).
- The effects of Cr substitution in these materials are investigated systematically.
- Initial discharge capacity of 342.7 mAh g^{-1} is obtained between 4.8 and 1.5 V when $x = 0.1$.
- The $x = 0.25$ sample exhibits the highest capacity retention of 92.93% after 50 cycles.
- Excessive Cr substitution may suppress the oxygen release from the lattice.

ARTICLE INFO

Article history:

Received 5 June 2013
Received in revised form
3 July 2013
Accepted 4 July 2013
Available online 17 July 2013

Keywords:
Lithium-ion battery
Cathode material
Iron–manganese oxide
Chromium substitution

ABSTRACT

Novel lithium-rich cathode materials, $\text{LiFe}_{1-x}\text{Cr}_x\text{O}_2 \cdot \text{Li}_2\text{MnO}_3$ ($x = 0, 0.1, 0.25, 0.5$), have been successfully synthesized using a co-precipitation method followed by hydrothermal and calcination treatment. The effects of Cr substitution on the structure and electrochemical properties of these materials are investigated. These composite materials with layered structure are mainly composed of agglomerated spherical particles with uniform particle size distribution. The sample with $x = 0.1$ delivers higher initial discharge capacity and higher initial Coulombic efficiency, which is believed to be associated with the oxidation of Cr^{3+} suggested by the CV curve. This sample also exhibits better rate capability than samples with other “ x ” values due to its low charge transfer resistance. The best cycling stability and highest reversible discharge capacity (226 mAh g^{-1} after 50 cycles) are obtained for the sample with $x = 0.25$. Excessive Cr substitution of Fe in the composite may suppress the oxygen release from Li_2MnO_3 on the first charging, which is helpful to stabilize the composite structure. This study not only provides a rational design approach for high-capacity cathode materials, but also demonstrates that the $\text{LiFe}_{1-x}\text{Cr}_x\text{O}_2 \cdot \text{Li}_2\text{MnO}_3$, is very attractive as cathode materials for lithium-ion batteries, providing that the amount of Cr substitution can be controlled appropriately.

© 2013 Elsevier B.V. All rights reserved.

1. Introduction

As attractive energy storage devices in cellular telephones and lap-top computers as well as applications for electric vehicles (EVs) and plug-in hybrid vehicles (PHEVs), lithium-ion batteries (LIBs) have been investigated worldwide for decades [1–3]. Since

carbon is used as negative electrodes in most of the commercial LIBs, lithium source is provided by the positive electrode material for Li extraction (charging) and insertion (discharging) processes associated with the oxidation and reduction of transition metal ions [4]. Therefore, rational design of the positive electrode material is critical and important for the application of lithium-ion batteries.

Owing to its easy preparation and stable electrochemical cycling performance, LiCoO_2 has been the dominant cathode material for lithium-ion batteries for almost two decades [5,6]. However, the further development of large-scale LIB production has been

* Corresponding author. Tel.: +86 10 68912508.

E-mail addresses: lily863@bit.edu.cn (L. Li), amine@anl.gov (K. Amine).

¹ Tel.: +1 630 252 3838.

impeded by the high cost of cobalt as well as the safety concerns of such batteries. In addition, to further reduce the weight, size and cost of battery packs for transportation applications, higher energy density cathode materials are quite important. Currently, the specific capacities of conventional cathode materials, such as layered LiCoO_2 [5,6] and $\text{LiMn}_{1/3}\text{Ni}_{1/3}\text{Co}_{1/3}\text{O}_2$ [7,8], olivine LiFePO_4 [9], and spinel LiMn_2O_4 [10,11], cannot entirely meet the energy density demands for the extended driving range of PHEVs. Therefore, the development of alternative low-cost cathode materials with high specific capacity becomes the inevitable trend.

In recent years, lithium-rich transition-metal oxides have been subjected to intensive investigation as they can deliver much higher capacities ($>250 \text{ mAh g}^{-1}$) at lower costs compared to the commercial LiCoO_2 cathodes. This class of materials can be described by several formulas, as $\text{Li}[\text{Li}_x\text{M}_{1-x}\text{O}_2]$ or $x\text{Li}_2\text{MnO}_3 \cdot (1-x)\text{LiMO}_2$ ($\text{M} = \text{Mn}$ [12], Co [13], Ni [14], Fe [15], Cr [16]). It has been reported that the substitution of Mn in Li_2MnO_3 by another 3d transition metal in these Li-rich composites offers higher potential with higher energy density than that of existing active materials. For instance, high initial discharge capacity of 281.1 mAh g^{-1} and high reversible capacity of 240.5 mAh g^{-1} were achieved for $\text{Li}/\text{Li}[\text{Li}_{0.2}\text{Co}_{0.13}\text{Ni}_{0.13}\text{Mn}_{0.54}]\text{O}_2$ cell tested between 2.0 and 4.8 V [17].

On another attempt to improve the capacity of the Li-rich composite, Tabuchi et al. have synthesized $\text{Li}_{1+x}(\text{Fe}_y\text{Mn}_{1-y})_{1-x}\text{O}_2$ (Fe-substituted Li_2MnO_3) cathode material based on the $\text{LiFeO}_2 \cdot \text{Li}_2\text{MnO}_3$ solid solution [18–20]. They found that the $\text{Fe}^{3+}/\text{Fe}^{4+}$ redox couple was observed in the 4 V region [15,18], indicating that Fe cation is effective as activator for leveraging a large amount of Li in Li_2MnO_3 . However, these materials suffered from poor cycle performance and low discharge voltage, although higher initial capacity was achieved. Partially substitution of Mn in Li_2MnO_3 by Ni [21,22] or Ti [23] in these composites could effectively improve the cycling stability and Coulombic efficiency of the cells. These studies opened a window to develop Fe-substituted Li_2MnO_3 -type layered cathode materials with improved electrochemical performance through simple doping or substitution by other transition metals. In this work, different amounts of Cr are employed to substitute Fe in $\text{LiFeO}_2 \cdot \text{Li}_2\text{MnO}_3$ to form the $\text{LiFe}_{1-x}\text{Cr}_x\text{O}_2 \cdot \text{Li}_2\text{MnO}_3$ ($x = 0, 0.1, 0.25, 0.5$) solid solutions (as shown in Fig. 1) for improving the electrochemical properties, by taking the advantage of the active $\text{Cr}^{3+}/\text{Cr}^{6+}$ couple [24–26], which not only contributes to the overall capacity, but also is capable of stabilizing the

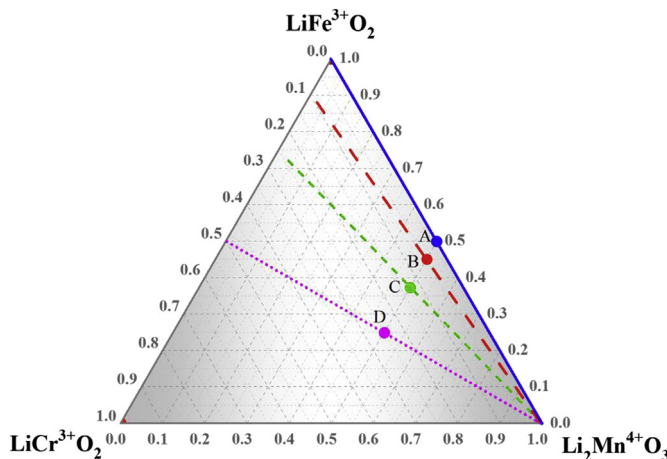


Fig. 1. Compositional phase diagram of lithium-excess Mn-based layered oxide: $\text{LiFe}^{3+}\text{O}_2$ – $\text{LiCr}^{3+}\text{O}_2$ – $\text{Li}_2\text{Mn}^{4+}\text{O}_3$ ($\text{LiFe}_{1-x}\text{Cr}_x\text{O}_2 \cdot \text{Li}_2\text{MnO}_3$). Points A, B, C and D in the triangular phase diagram represent $\text{LiFeO}_2 \cdot \text{Li}_2\text{MnO}_3$ ($x = 0$), $\text{LiFe}_{0.9}\text{Cr}_{0.1}\text{O}_2 \cdot \text{Li}_2\text{MnO}_3$ ($x = 0.1$), $\text{LiFe}_{0.75}\text{Cr}_{0.25}\text{O}_2 \cdot \text{Li}_2\text{MnO}_3$ ($x = 0.25$) and $\text{LiFe}_{0.5}\text{Cr}_{0.5}\text{O}_2 \cdot \text{Li}_2\text{MnO}_3$ ($x = 0.5$), respectively.

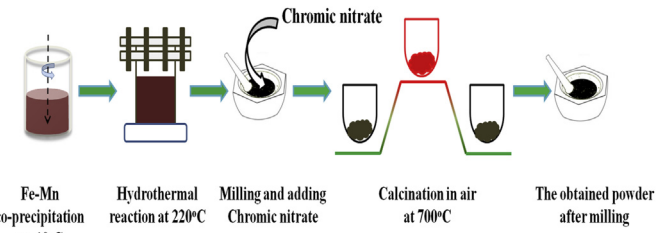


Fig. 2. Flow diagram of the synthesis process of $\text{LiFe}_{1-x}\text{Cr}_x\text{O}_2 \cdot \text{Li}_2\text{MnO}_3$.

composite structure. Consequently, the electrochemical performance of the synthesized $\text{LiFe}_{1-x}\text{Cr}_x\text{O}_2 \cdot \text{Li}_2\text{MnO}_3$ as the cathode material is significantly improved. The influence of Cr substitution on the structures, morphologies, and electrochemical properties of $\text{LiFe}_{1-x}\text{Cr}_x\text{O}_2 \cdot \text{Li}_2\text{MnO}_3$ are studied systematically.

2. Experimental

2.1. Materials synthesis

In this work, all the chemicals were of analytical grade and used as-received without further purification. All homogeneous $\text{LiFe}_{1-x}\text{Cr}_x\text{O}_2 \cdot \text{Li}_2\text{MnO}_3$ ($x = 0, 0.1, 0.25, 0.5$) samples were synthesized using a three-step process comprising co-precipitation, hydrothermal reaction and calcination in air, as described in Fig. 2.

- (1) *Fe–Mn co-precipitation:* $\text{Fe}(\text{NO}_3)_3 \cdot 9\text{H}_2\text{O}$, $\text{MnCl}_2 \cdot 4\text{H}_2\text{O}$ and $\text{LiOH} \cdot \text{H}_2\text{O}$ were used as starting chemicals. The Fe–Mn coprecipitate was prepared by slowly dropping Fe–Mn mixed solution into $\text{LiOH} \cdot \text{H}_2\text{O}$ solution under magnetically stirring for 3 h at -10°C . An appropriate amount of ethanol was added to avoid freezing of the solution at -10°C . The as-obtained solution was subjected to aging with stirring overnight at room temperature. Filtration process was employed to isolate the Fe–Mn coprecipitate for the next hydrothermal treatment.
- (2) *Hydrothermal treatment:* A certain amount of KOH, $\text{LiOH} \cdot \text{H}_2\text{O}$ and KClO_3 were mixed with the Fe–Mn coprecipitate in distilled water. Then the mixed suspension was transferred into a 100 mL polytetrafluoroethylene (PTFE) reactor at 220°C for 48 h, allowing for hydrothermal reaction taking place. After

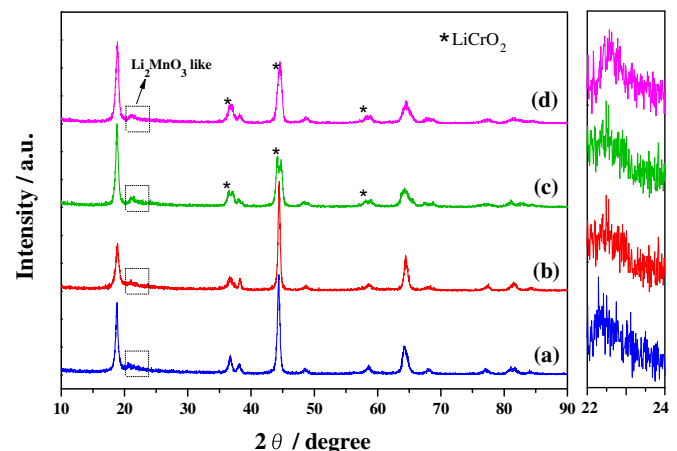


Fig. 3. XRD patterns of as-prepared samples ($\text{LiFe}_{1-x}\text{Cr}_x\text{O}_2 \cdot \text{Li}_2\text{MnO}_3$): (a) $x = 0$, (b) $x = 0.1$, (c) $x = 0.25$, (d) $x = 0.5$.

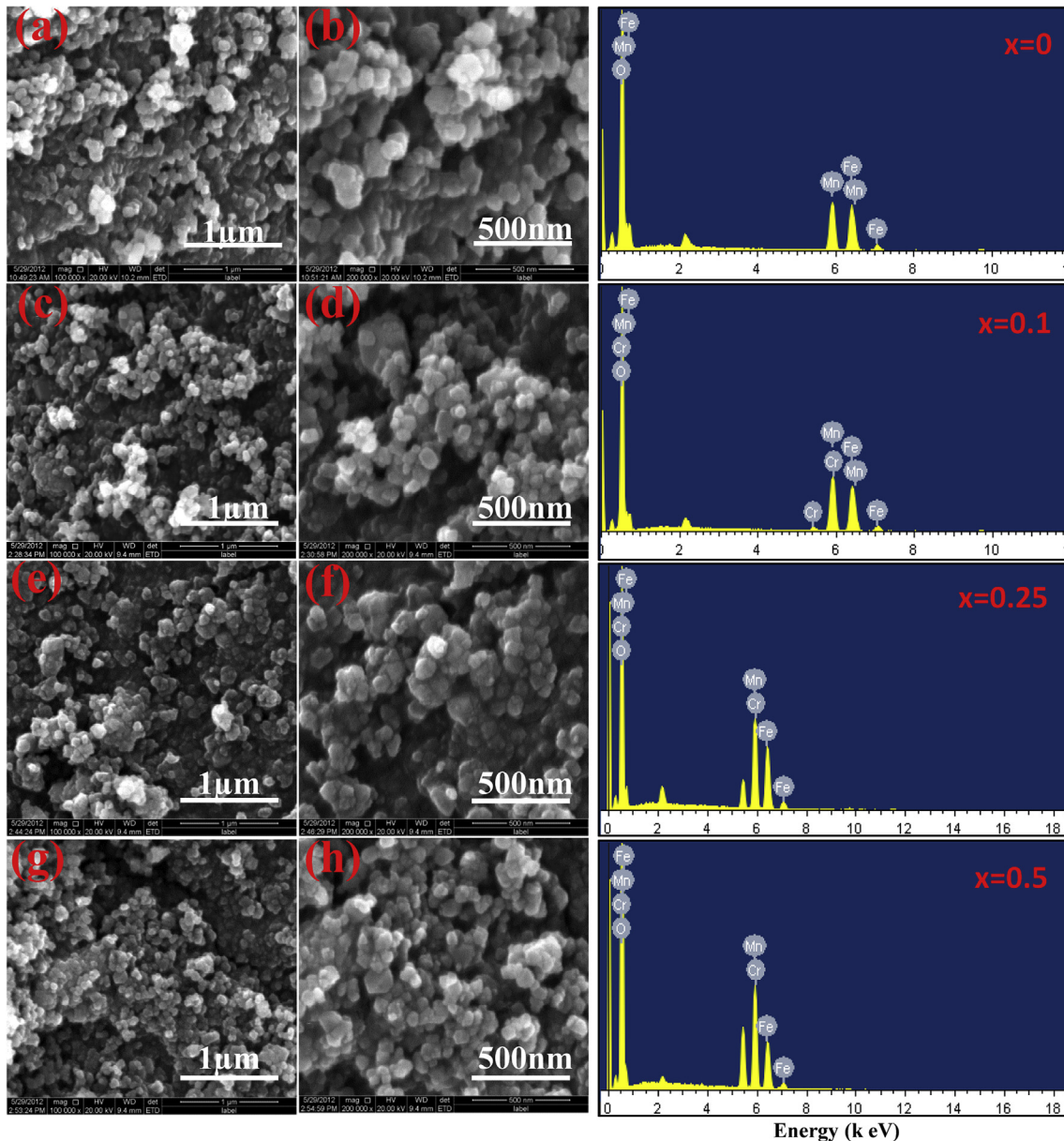


Fig. 4. Scanning electron micrographs of $\text{LiFe}_{1-x}\text{Cr}_x\text{O}_2 \cdot \text{Li}_2\text{MnO}_3$ under different magnifications of $\times 100$ k and $\times 200$ k: $x = 0$ (a and b), $x = 0.1$ (c and d), $x = 0.25$ (e and f), $x = 0.5$ (g and h). The right section is the corresponding EDX spectra of as-prepared samples.

isolated by repeated washing with distilled water and then dried overnight, the low-crystallinity sample was obtained.

(3) *Calcination process:* The low-crystallinity sample was mixed with 100 mL of $\text{LiOH} \cdot \text{H}_2\text{O}$ solution. After drying at 100 °C overnight and grinding, the mixture was calcined in air at 700 °C for 20 h. Excess amount of lithium hydroxide was eliminated from the sample by rinsing with distilled water and subsequent drying.

The addition of $\text{Cr}(\text{NO}_3)_3 \cdot 9\text{H}_2\text{O}$ was performed before the calcination step, because Cr^{3+} ion will be dissolved into the solution under high pH condition.

2.2. Materials characterizations

The crystalline structures of all the samples were characterized using X-ray diffraction (XRD; Rigaku Ultima IV–185) with a $\text{Cu K}\alpha$

radiation source. The source tension and current are 40 kV and 40 mA, respectively. Data were acquired with a scan rate of 8° min^{-1} over a 2θ range of 10° – 90° . Morphological studies and element ratio tests on the samples were performed using a field emission scanning electron microscope (SEM, FEI, Quanata 200f) with an accelerating voltage of 20 kV and an energy dispersive X-ray detector.

Table 1

The chemical formula, designed values and measured values of as-prepared samples.

Sample x	Chemical formula $\text{LiFe}_{1-x}\text{Cr}_x\text{O}_2 \cdot \text{Li}_2\text{MnO}_3$	Theoretical			Measured		
		Fe	Cr	Mn	Fe	Cr	Mn
$x = 0$	$\text{Li}_{1.2}\text{Fe}_{0.4}\text{Mn}_{0.4}\text{O}_2$	0.4	0	0.4	0.3965	0	0.4035
$x = 0.1$	$\text{Li}_{1.2}\text{Fe}_{0.36}\text{Cr}_{0.04}\text{Mn}_{0.4}\text{O}_2$	0.36	0.04	0.4	0.3533	0.0375	0.4092
$x = 0.25$	$\text{Li}_{1.2}\text{Fe}_{0.3}\text{Cr}_{0.1}\text{Mn}_{0.4}\text{O}_2$	0.3	0.1	0.4	0.2921	0.1035	0.4044
$x = 0.5$	$\text{Li}_{1.2}\text{Fe}_{0.2}\text{Cr}_{0.2}\text{Mn}_{0.4}\text{O}_2$	0.2	0.2	0.4	0.2033	0.2055	0.3912

2.3. Electrochemical measurements

The working electrode for electrochemical measurements was prepared by dispersing the as-synthesized active material, acetylene black and polyvinylidene fluoride (PVDF) at a weight percent ratio of 8:1:1 in the solvent of *N*-methyl-2-pyrrolidone (NMP). Then the slurry was cast on an aluminum foil using automatic film-coating equipment and dried overnight in a vacuum oven at 80 °C. The electrode was further roll-pressed in order to enhance interparticle contact and promote adhesion to the current collector. Electrochemical measurements were performed using galvanostatic cycling with two-electrode coin-cells (type CR 2025). Cell assembly was carried out in an Ar-filled glove box, using the prepared electrode, metallic lithium foil as the counter electrode, 1 M LiPF₆ dissolved in ethyl carbonate (EC) and dimethyl carbonate (DMC) (1:1 by volume) as the electrolyte, and a Celgard 2400 membrane as the separator. Galvanostatic charge–discharge tests were all performed under constant current conditions using Land battery testers (Land CT2001A, Wuhan, China). The assembled cells were measured for 50 cycles at a current density of 0.1 C (20 mA g⁻¹) to analyze the cycling performances of the materials. Various rates (0.1, 0.2, 0.5, 1.0, and 2.0 C) were tested to investigate the rate capabilities of the prepared materials. It should be pointed out that a two-step charge process was employed. That is, the constant current charge step was followed by an additional constant voltage charge step till the current density dropped to one fourth of its initial value.

Cyclic voltammetry (CV; 2–5 V, 0.1 mV s⁻¹) measurements were performed on a CHI660C electrochemical workstation. Electrochemical impedance spectroscopy (EIS) analysis was carried out from 10⁵ Hz to 0.01 Hz using an IM6 electrochemical impedance analyzer with an AC perturbation signal of 5 mV. The potentials throughout the paper are referenced to the Li/Li⁺ couple.

3. Results and discussion

3.1. Structural characterizations

XRD was performed to investigate the phase structures of the samples. Fig. 3 shows the XRD patterns of the as-prepared LiFe_{1-x}Cr_xO₂·Li₂MnO₃ samples with different *x* values. The good crystalline natures of the synthesized samples are indicated by the well-defined diffraction patterns. The layered rock-salt form with hexagonal α -NaFeO₂-type structure with a space group of $R\bar{3}m$ is detected on each XRD pattern. A low intensity peak near $2\theta = 21^\circ - 23^\circ$ (enlarged in the right panel of Fig. 3) for each pattern arises from sublattice ordering of Li and Mn in the transition-metal-containing layer, which is the characteristic of a Mn-rich sample close to the Li₂MnO₃ composition, corresponding to the C/2m structure [27–29]. Some additional peaks corresponding to LiCrO₂ are also observed in the patterns of *x* = 0.25 and *x* = 0.5. In addition, the 003 ($2\theta = 19^\circ$) to 104 ($2\theta = 43^\circ$) peak ratio increases with increasing *x* value, indicating the improvement of layered structure.

3.2. Morphologies and EDX spectra of the samples

Field emission scanning electron microscopy (FESEM) images of the particles collected after calcination process are presented in Fig. 4. The obtained powders with different compositions are observed to be agglomerated with relatively spherical particles of <100 nm. The particle size for the *x* = 0.1 sample appears to be smaller than those for the other three. Such uniform crystal morphology with small particle size is beneficial to provide sufficient contact between the oxide material and the electrolyte to promote electrochemical reactions.

EDX spectroscopy was employed to investigate the compositions of obtained powders, as shown in the right section of Fig. 4. All the synthesized samples are composed of the expected elements with the content of each element close to that in the designed formula (see Table 1), indicating that the composition of the samples are well controlled by our synthetic method employed in this study.

3.3. Initial charge and discharge properties

Fig. 5 compares the first charge/discharge profiles and the corresponding differential capacity versus voltage (dQ/dV^{-1}) plots for all samples at 0.1 C rate. In the first charge profile, the *x* = 0 and *x* = 0.1 samples are similar in terms of curve shapes, which showed a slope below 4.4 V and a plateau above 4.4 V. A notable change occurs when the samples reached higher Cr content (*x* = 0.25 and *x* = 0.5 sample),

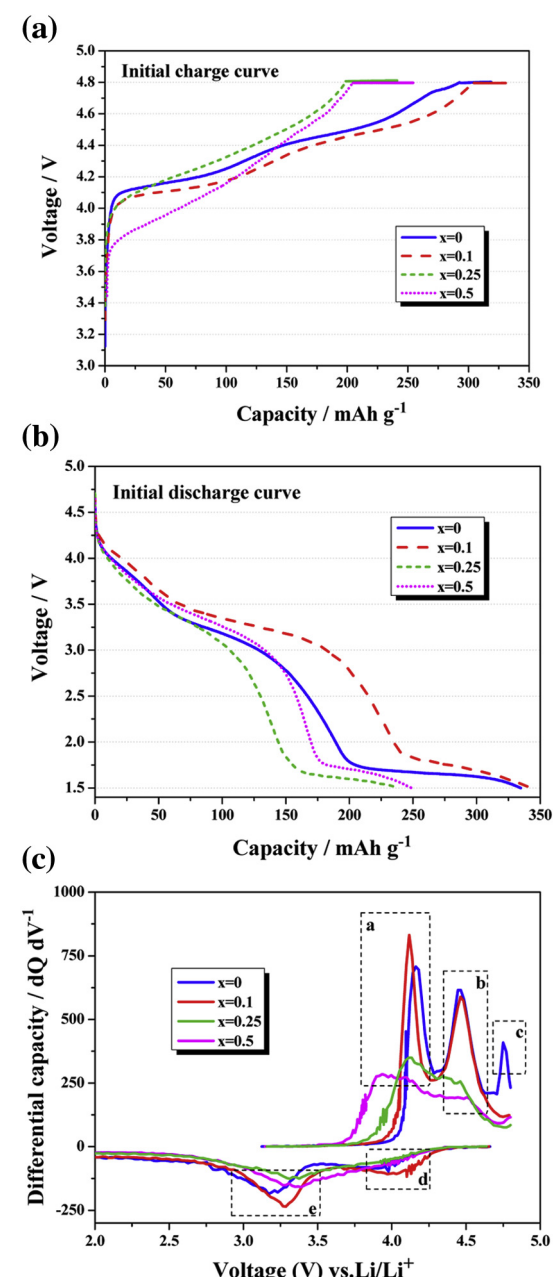


Fig. 5. Initial (a) charge and (b) discharge curves and (c) corresponding initial charge/discharge cycle differential capacity versus voltage plots of the samples.

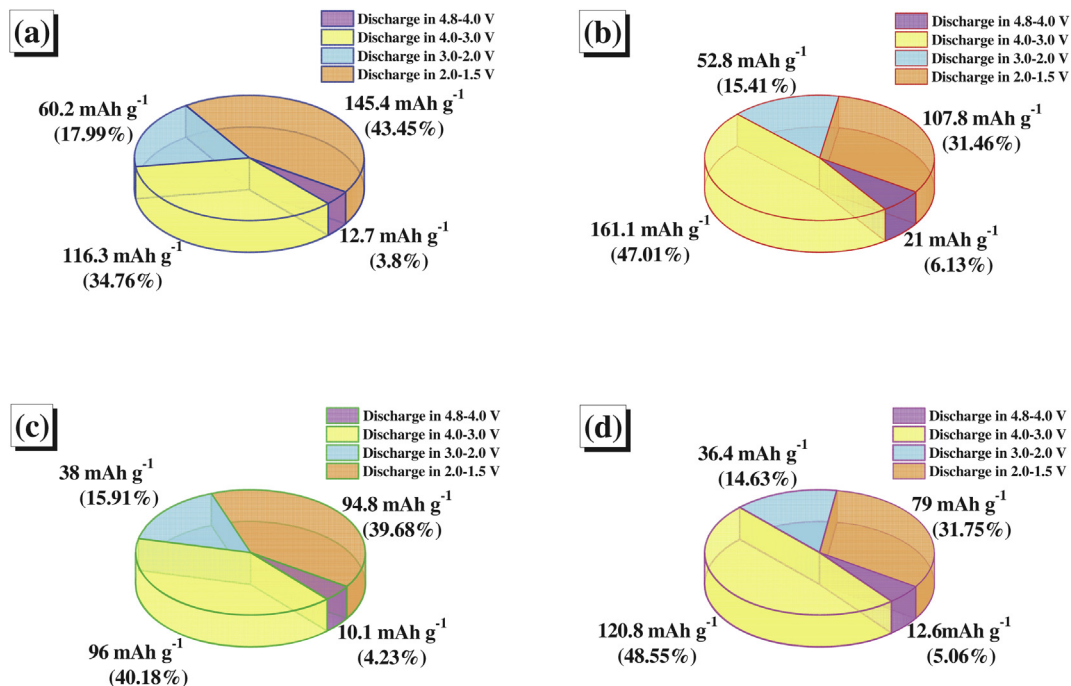


Fig. 6. 3D pie charts of initial discharge capacities and proportions in different voltage ranges of as-prepared samples $\text{LiFe}_{1-x}\text{Cr}_x\text{O}_2 \cdot \text{Li}_2\text{MnO}_3$: (a) $x = 0$, (b) $x = 0.1$, (c) $x = 0.25$, (d) $x = 0.5$.

i.e., there is no obvious boundary line of the two charge plateaus around 4.4 V. During discharging, all the samples show the same trend with two long discharge plateaus at 3.3 V and below 2.0 V.

The sample without Cr substitution delivers an initial charge capacity of 318.8 mAh g^{-1} , but suffers from a large irreversible capacity loss of 129.6 mAh g^{-1} when discharging the cell to 2.0 V. However, when the cell is discharged to 1.5 V, a long plateau occurs at around 1.7 V, which provides additional discharge capacity of 145.4 mAh g^{-1} . The first cycle Coulombic efficiency is improved from 59% in the voltage window of 4.8–2 V to 105% of 4.8–1.5 V. After adding small amount of Cr ion, the initial discharge capacity and Coulombic efficiency of the $x = 0.1$ sample are greatly improved, as shown in Fig. 5. The sample with $x = 0.1$ delivers higher discharge capacities of 234.9 mAh g^{-1} between 4.8 and 2.0 V and 342.7 mAh g^{-1} between 4.8 and 1.5 V, respectively, compared to those for the sample without Cr substitution. As displayed in Fig. 6, the enhanced discharge capacity for the Cr-substituted sample mainly comes from the voltage window of 4.8–2.0 V, more particularly between 4.0 and 3.0 V. This leads to a higher initial Coulombic efficiency (71%) in the voltage range of 2.0–4.8 V compared to that of the sample with $x = 0$ (59%), as listed in Table 2. However, adding more amount of Cr ion results in decreased initial charge and discharge capacities, although initial Coulombic efficiencies in 2.0–4.8 V are improved compared to the sample without Cr substitution.

In order to investigate the specific regions of the enhanced initial discharge capacity, the detailed information during

different voltage ranges has been calculated. The charts in Fig. 6 show that the discharge capacities and the corresponding proportions in the voltage range of 3.0–4.0 V (yellow color, in web version) and 4.0–4.8 V (purple color, in web version) of the $x = 0.1$ sample are higher than those of the $x = 0$ sample. It is clearly seen that the enhanced capacity by small amount of Cr substitution is mainly promoted in the voltage range of 3.0–4.0 V, from 116.3 mAh g^{-1} (34.76%) to 161.1 mAh g^{-1} (47.01%). In addition, it should be pointed out that the initial discharge capacity in 2.0–1.5 V decreases with the increasing x value, from 145.4 mAh g^{-1} to 79 mAh g^{-1} , as can be found in Fig. 6 (orange color, in web version) and Table 2. This indicates that the long discharge plateau between 2.0 and 1.5 V is associated with the electrochemical reduction of Fe ion.

To further understand the detail electrochemical reactions in the first charge/discharge process, differential capacity versus voltage plots of the samples are illustrated in Fig. 5(c). As for the sample with $x = 0$, the oxidation peak at 4.2 V is corresponding to the oxidation of Fe^{3+} to Fe^{4+} . It also can be found that the peak positions in section “a” move towards left with the increasing x value, which may be associated with the electrochemical oxidation of Cr^{3+} to Cr^{6+} around 3.8 V. Section “b” is mainly attributed to a loss of oxygen from the layered lattice and, at the same time, the

Table 2
Initial charge and discharge data of as-prepared samples.

Sample	$Q_{1c} (\text{mAh g}^{-1})$		$Q_{1d} (\text{mAh g}^{-1})$		$Q_{1d}/Q_{1c} (\%)$		
	4.5 V	4.8 V	4.8–2.0 V	4.8–1.5 V	2.0–1.5 V	2.0–4.8 V	1.5–4.8 V
$x = 0$	203.8	318.8	189.2	334.6	145.4	59.03	104.96
$x = 0.1$	228.1	330.7	234.9	342.7	107.8	71.03	103.63
$x = 0.25$	148.9	241.2	144.1	238.9	94.8	59.74	99.05
$x = 0.5$	163	254.4	169.8	248.8	79.0	66.75	97.80

Table 3
Bond dissociation energies of metal–oxygen bonds.

M	M–O bond energy ΔH_{298}^a (kJ mol ⁻¹)
Li	341(6)
Fe	409(13)
Cr	427(29)
Mn	402(34)
Co	368(21)
Ni	391.6(38)
Al	512(4)
Ti	662(16)

^a Bond dissociation energies are defined as the standard enthalpy change for the reaction $\text{AB} \rightarrow \text{A} + \text{B}$ at 298 K.

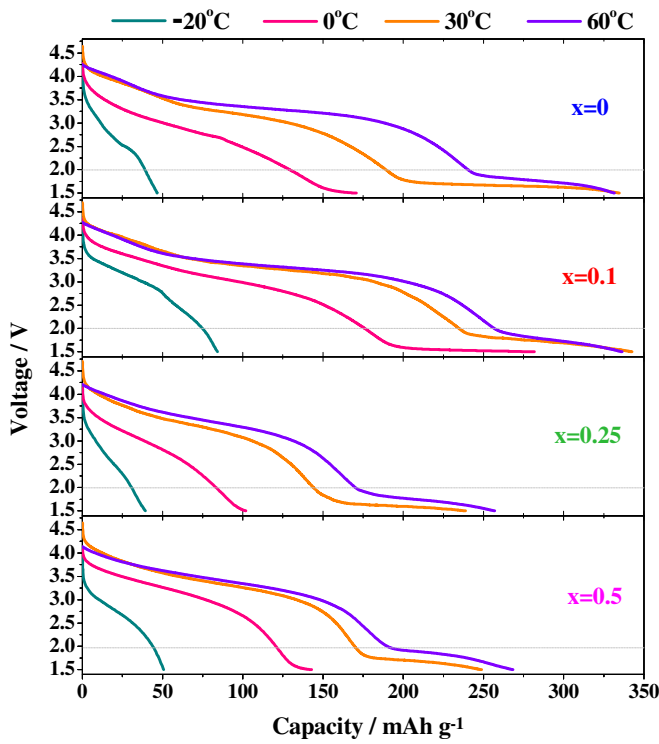


Fig. 7. High- and low-temperature behaviors of $\text{Li}/\text{LiFe}_{1-x}\text{Cr}_x\text{O}_2 \cdot \text{Li}_2\text{MnO}_3$ half-cells ($x = 0, 0.1, 0.25, 0.5$).

electrochemical activation of Li_2MnO_3 component above 4.4 V [30]. As for the $x = 0.25$ sample and the $x = 0.5$ sample, the peaks above 4.4 V become indistinct, indicating that the excessive Cr ions may suppress the oxidation of the O^{2-} ions to O_2 , and reduce the extraction of Li_2O from the Li_2MnO_3 component. In section “d”, the $x = 0.1$ sample has a more evident peak at 4.0 V than the other samples, which is due to the reduction of Fe^{4+} to Fe^{3+} . Section “e” shows the formation of spinel structure, corresponding to the

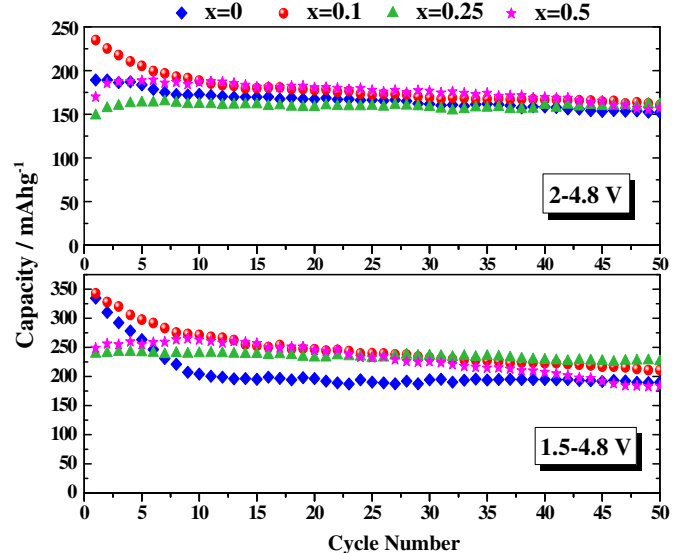


Fig. 9. Discharge capacities of the $\text{Li}/\text{LiFe}_{1-x}\text{Cr}_x\text{O}_2 \cdot \text{Li}_2\text{MnO}_3$ half-cells ($x = 0, 0.1, 0.25, 0.5$) with different discharge cut-off voltages.

reduction of Mn^{4+} to Mn^{3+} around 3.3 V, which is triggered by the electrochemical activation of Li_2MnO_3 in the first charge process. At the same time, the reduction of Cr^{6+} to Cr^{3+} may be overlapped in section “e”. It should be also noted that the peak around 4.75 V in section “c”, which is only observed in the $x = 0$ sample, may be related to the decomposition of the electrolyte.

When the Cr content changes from $x = 0.1$ to $x = 0.25$, as the oxygen loss suppressed, the discharge capacity also decreases rapidly with increasing Cr content. With an aim to understand the origin of the variations in the oxygen loss plateau with Cr substitution, we have considered the bond energies of the metal–oxygen bonds. The Cr–O bond is stronger than the Mn–O bond, which is revealed by the bond dissociation energy ΔH_f values given in Table 3 [31]. The stronger binding of oxygen to Cr could be

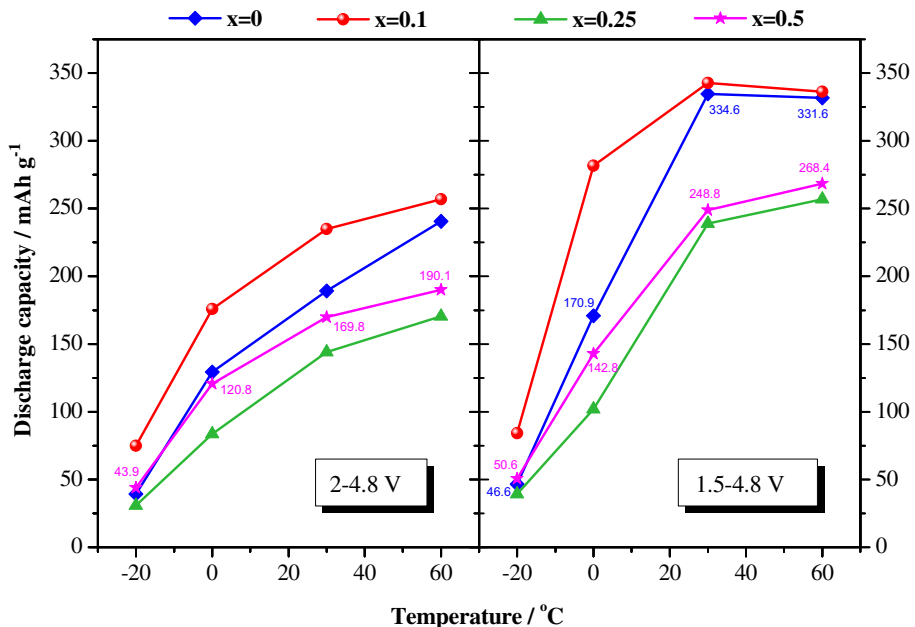


Fig. 8. High- and low-temperature discharge capacities data of $\text{Li}/\text{LiFe}_{1-x}\text{Cr}_x\text{O}_2 \cdot \text{Li}_2\text{MnO}_3$ half-cells ($x = 0, 0.1, 0.25, 0.5$).

considered to suppress the release of oxygen from the lattice, indicating that the binding of oxygen to metal ions may play an important role in the degree of oxygen loss. Although excessive substitution with Cr^{3+} has a negative effect on the capacity of lithium-rich high-capacity layered oxides, the substitution may generally improve the structure stability of the cathode materials, and therefore, the cyclability of the cell.

3.4. High- and low-temperature behaviors

High- and low-temperature discharge characteristics are presented in Fig. 7 and the data with different cut-off voltages are compared in Fig. 8. It can be found that the discharge capacities of all the samples present an overall upward trend with the increasing temperature on discharging to 2.0 V. However, there is a slightly decrease of the discharge capacities from 30 °C to 60 °C for the samples with $x = 0$ and $x = 0.1$ when the cells discharging to 1.5 V, ascribing to the reduced discharge capacities in the voltage range of 2.0–1.5 V. In short, the sample with $x = 0.1$ exhibits the highest discharge capacities in all different temperatures tested than the others.

3.5. Cycling performances

The cycling performances of all the samples in two voltage ranges of 2–4.8 V and 1.5–4.8 V are compared in Fig. 9. In 1.5–4.8 V, it can be seen that the discharge capacities of all the samples

gradually reduce during the earlier cycles and then become stable. In the case of the sample with $x = 0.1$, although it delivers the highest initial discharge capacity, its capacity fade is faster, which is possibly due to the structure instability with small amount of Cr substitution. On the other hand, the sample with $x = 0.25$ has the highest capacity retention (92.93% of initial value) and the highest reversible discharge capacity after 50 cycles (226 mAh g⁻¹). This could be attributed to the excessive Cr substitution in this sample, which effectively restrains the release of oxygen from Li_2MnO_3 and keeps a better layered structure, leading to the best charge/discharge cycle stability. In addition, in the voltage range of 2.0–4.8 V, the similar trend of discharge capacities of the samples is also observed, indicating that there could be almost no structure damage when the samples are worked at a lower cut-off voltage of 1.5 V. It is obvious that the long-term cyclic performance can be improved by Cr substitution, and the $x = 0.25$ sample appears to have the highest reversible discharge capacity and best cycling performance.

3.6. Rate capability

Fig. 10 compares the initial discharge profiles at various C rates of all the samples to evaluate their rate capabilities. The graph in Fig. 10(e) clearly illustrates the detailed change tendency of the discharge capacities in different discharge voltage ranges. The initial discharge capacities of all the samples progressively decrease with the increasing current density, ascribing to the reduced time for Li^+ intercalation into the crystal lattice when the electrodes discharged at high current densities [21]. The results in Fig. 10 clearly show that the sample with $x = 0.1$ has higher stable discharge capacities at various rates (339 mAh g⁻¹ at 0.2 C, 329.9 mAh g⁻¹ at 0.5 C, 310.5 mAh g⁻¹ at 1 C and 263 mAh g⁻¹ at 2 C) than the other samples. Once again, the enhanced discharge capacity mainly comes from the voltage range of 2.0–4.8 V.

Another rate capability test was carried out to further demonstrate the advantage of Cr substitution, as shown in Fig. 11. In this test, the cell was first charged by a two-step charge process between 1.5 and 4.8 V with a current density of 20 mA g⁻¹ (0.1 C-rate) before each discharge, and then discharged at increasing rates for 5 cycles at current densities from 20 mA g⁻¹ (0.1 C-rate) to 400 mA g⁻¹ (2 C-rate). In general, the capacity retention of all samples declines with the increasing rate. It is clear that, except for 0.1 C-rate, the samples with Cr substitution exhibit higher discharge capacities than that without Cr substitution (the

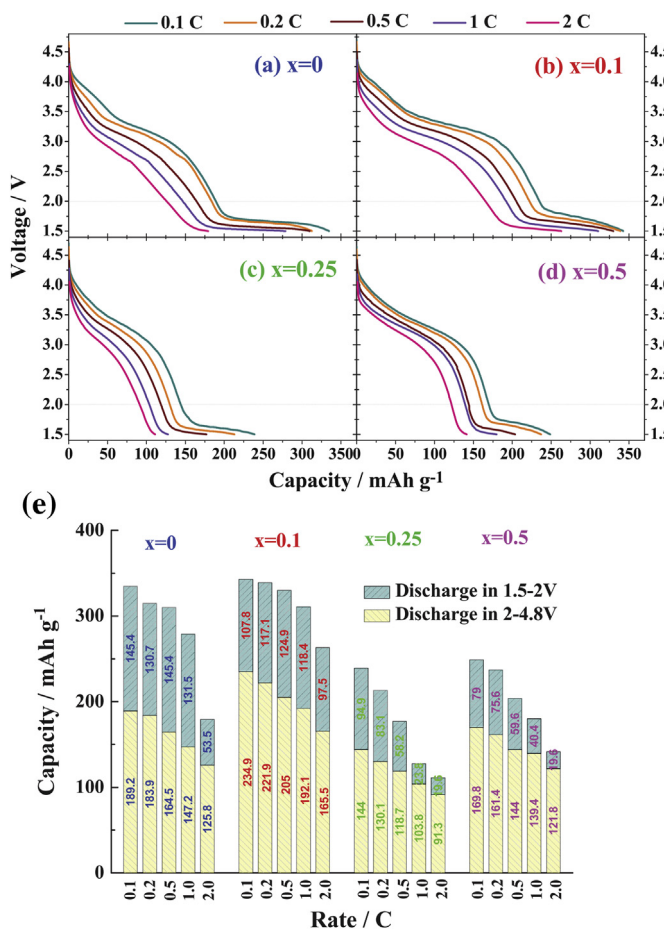


Fig. 10. Initial rate capabilities of the $\text{Li}/\text{LiFe}_{1-x}\text{Cr}_x\text{O}_2 \cdot \text{Li}_2\text{MnO}_3$ half-cells at various rates. (a) $x = 0$, (b) $x = 0.1$, (c) $x = 0.25$, (d) $x = 0.5$, (e) detailed data of initial discharge capacities.

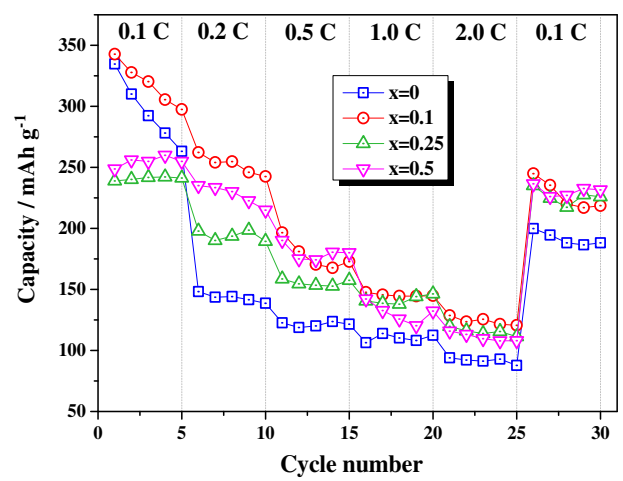


Fig. 11. Rate capabilities of the $\text{Li}/\text{LiFe}_{1-x}\text{Cr}_x\text{O}_2 \cdot \text{Li}_2\text{MnO}_3$ half-cells ($x = 0, 0.1, 0.25, 0.5$) at various C rates.

$x = 0$ sample) at all rates. At 2 C-rate, the average discharge capacity is 125.5 mAh g^{-1} for the $x = 0.1$ sample, while only 92.2 mAh g^{-1} for the $x = 0$ sample. After 2 C-rate, the discharge capacity of the $x = 0.1$ sample can again reach 220 mAh g^{-1} at 0.1 C, about 64.2% of its initial discharge capacity. In short, the $x = 0.1$ sample presents more stable rate capability, indicating that appropriate amount of Cr substitution also improves the rate capability compared with the sample without Cr substitution.

3.7. Cyclic voltammetry

Cyclic voltammetry was carried out in the voltage range of 2.0–5.0 V for 5 cycles at a scan rate of 0.1 mV s^{-1} to further understand

the effect of Cr substitution on the electrochemical properties of $\text{LiFe}_{1-x}\text{Cr}_x\text{O}_2 \cdot \text{Li}_2\text{MnO}_3$. The typical CV curves of all the samples are shown in Fig. 12. As can be seen, for all the samples, there is an anodic peak centered at about 4.3 V and a reduction peak at 4.0 V in the first cycle, corresponding to the redox of $\text{Fe}^{3+}/\text{Fe}^{4+}$ [15,18,32]. It can be found that the reduction peak at 4.0 V gradually weakens with the increasing content of Cr substitution. Meanwhile, the oxidation peak around 4.6 V, corresponding to the extraction of Li_2O and the electrochemical activation of Li_2MnO_3 [30], also weakens with the increasing x value, which implies that the Cr substitution of Fe suppress the loss of oxygen from the composite. The reduction peaks around 3.3 V, ascribing to the redox of $\text{Mn}^{4+}/\text{Mn}^{3+}$, come from the electrochemical activation of Li_2MnO_3 [24].

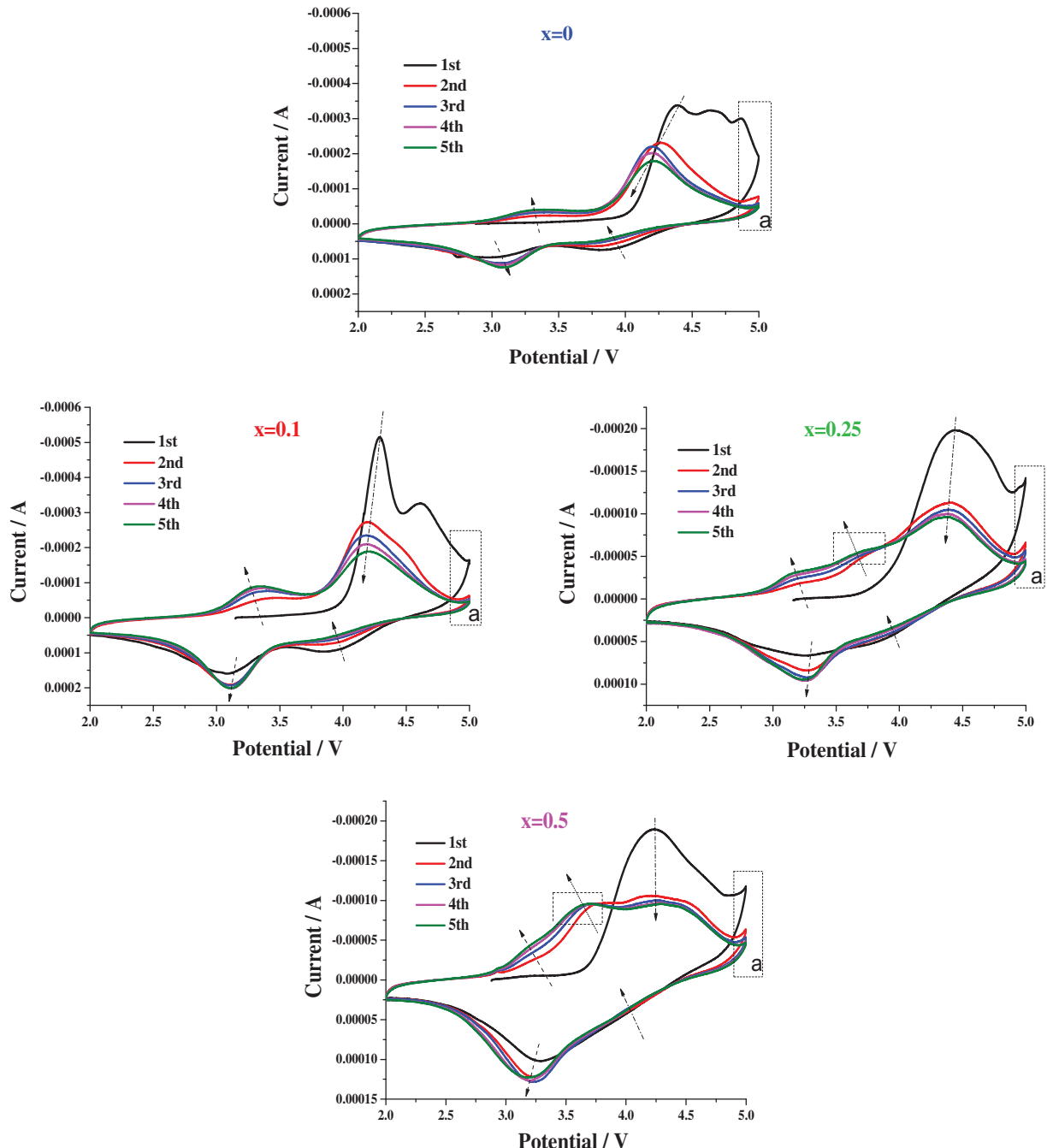


Fig. 12. CV curves of the $\text{Li}/\text{LiFe}_{1-x}\text{Cr}_x\text{O}_2 \cdot \text{Li}_2\text{MnO}_3$ half-cells ($x = 0, 0.1, 0.25, 0.5$).

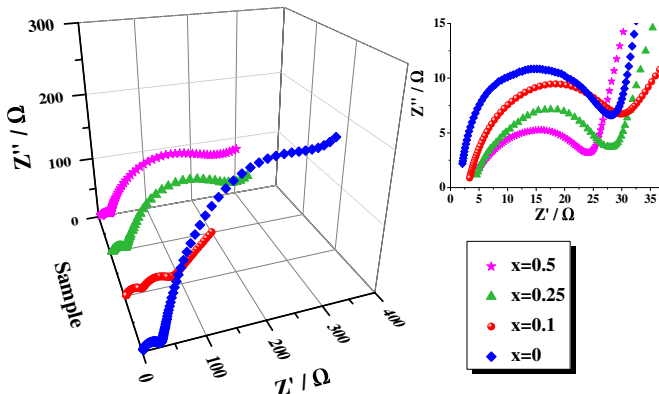


Fig. 13. AC impedance spectra of the $\text{Li}/\text{LiFe}_{1-x}\text{Cr}_x\text{O}_2\cdot\text{Li}_2\text{MnO}_3$ half-cells ($x = 0, 0.1, 0.25, 0.5$).

Interestingly, after the first cycle, an oxidation peak at 3.7 V appears and increases with cycles for samples with $x = 0.25$ and $x = 0.5$, and this could be associated to the oxidation of Cr^{3+} to Cr^{6+} [24,26]. Its corresponding reduction peak may be overlapped with the reduction peak at about 3.3 V. The peaks in section "a" may be related to the decomposition of the electrolyte. In addition, the good reversible performance can be known from the overlap states after the first cycle.

3.8. Electrochemical impedance analysis

To analyze the differences in the polarization behaviors and understand the distinction in rate capability, ac impedance spectra of all the samples charged to 4.3 V at the fourth cycle were measured (Fig. 13). The right part of Fig. 13 displays the enlarged spectra at the high frequency. In general, the semicircle in the high-frequency section relates to the resistance for Li^+ migration through the SEI layer (R_{SEI}), the semicircle in the medium-frequency section is assigned to the charge transfer resistance between the SEI layer and electrode interface (R_{ct}), and the rising line in the low-frequency section is attributed to Warburg impedance. The intercept of the semicircle at the highest frequency with the horizontal axis (Z') refers to the uncompensated ohmic resistance (R_{Ω}). The total cell resistance (R_{total}), consisting of R_{Ω} , R_{SEI} and R_{ct} , reflects the electrochemical stability and the kinetics of cell reaction [33,34]. As can be seen clearly, the $x = 0.1$ sample exhibits a smaller R_{total} than the other samples, so its excellent cell performance is probably related to its high electrochemical stability. Especially, the $x = 0.1$ sample and the $x = 0.25$ sample possess smaller R_{ct} and almost the same R_{SEI} compared with the other two samples, indicating the good electrical contact among the particles. Therefore, according to the EIS analysis, the optimal electrochemical kinetic of the $\text{LiFe}_{1-x}\text{Cr}_x\text{O}_2\cdot\text{Li}_2\text{MnO}_3$ electrode is achieved when $x = 0.1$ and $x = 0.25$, which is in good agreement with the charge–discharge performances of the samples.

4. Conclusion

A co-precipitation method followed by hydrothermal reaction and then calcination process has been demonstrated for the synthesis of cathode material $\text{LiFe}_{1-x}\text{Cr}_x\text{O}_2\cdot\text{Li}_2\text{MnO}_3$ ($x = 0, 0.1, 0.25, 0.5$). In contrast to the Fe-substituted Li_2MnO_3 , Cr substitution samples can act as potential positive electrodes with high reversible discharge capacity ($>220 \text{ mAh g}^{-1}$) as other lithium-rich layered oxide cathodes like $\text{LiNi}_{1/3}\text{Mn}_{1/3}\text{Co}_{1/3}\text{O}_2\cdot\text{Li}_2\text{MnO}_3$, if the amount of Cr substitution could be adjusted suitably. The

composition $\text{LiFe}_{0.9}\text{Cr}_{0.1}\text{O}_2\cdot\text{Li}_2\text{MnO}_3$ ($x = 0.1$) exhibits the highest initial charge and discharge capacities and the best rate capability, while the highest discharge capacity retention and the highest reversible discharge capacity (226 mAh g^{-1} after 50 cycles) are obtained with $\text{LiFe}_{0.75}\text{Cr}_{0.25}\text{O}_2\cdot\text{Li}_2\text{MnO}_3$ ($x = 0.25$). Excessive Cr substitution has been found to suppress the oxidation of O^{2-} ions to O_2 and further reduce the oxygen loss from the lattice during the first charge process. The suppression of oxygen loss could be attributed to the stronger binding of oxygen with Cr (higher bond dissociation energy). Reducing the amount of Fe ion, namely increasing the amount of Cr substitution, is necessary and effective to reduce Li_2O extraction on initial charging, leading to better layered structure stability. Cr-substituted $\text{LiFeO}_2\cdot\text{Li}_2\text{MnO}_3$ is attractive as a positive electrode material in lithium-ion batteries if the amount of Cr substitution could be controlled in a reasonable range.

Acknowledgments

The experimental work of this study was supported by the International S&T Cooperation Program of China (2010DFB63370), the Chinese National 973 Program (2009CB220106), Beijing Nova Program (Z121103002512029), Beijing Excellent Talents Plan funding and the New Century Educational Talents Plan of the Chinese Education Ministry (NCET-12-0050). Argonne National Laboratory, a U.S. Department of Energy Office of Science laboratory, is operated under Contract No. DE-AC02-06CH11357.

References

- [1] J. Li, J.M. Zheng, Y. Yang, *J. Electrochem. Soc.* 154 (2007) A427–A432.
- [2] J.M. Zheng, J. Li, Z.R. Zhang, X.J. Guo, Y. Yang, *Solid State Ionics* 179 (2008) 1794–1799.
- [3] X.Y. Zhang, W.J. Jiang, A. Mauger, R. Qilu, F. Gendron, C.M. Julien, *J. Power Sources* 195 (2010) 1292–1301.
- [4] J.B. Goodenough, Y. Kim, *Chem. Mater.* 22 (2010) 587–603.
- [5] N. Ding, X.W. Ge, C.H. Chen, *Mater. Res. Bull.* 40 (2005) 1451–1459.
- [6] E. Grigorova, T.S. Mandzhukova, M. Khristov, M. Yoncheva, R. Stoyanova, E. Zhecheva, *J. Mater. Sci.* 46 (2011) 7106–7113.
- [7] X.J. Liu, G.Y. Zhu, K. Yang, J.Q. Wang, *J. Power Sources* 174 (2007) 1126–1130.
- [8] Y.S. He, L. Pei, X.Z. Liao, Z.F. Ma, *J. Fluorine Chem.* 128 (2007) 139–143.
- [9] H.G. Deng, S.L. Jin, L. Zhan, Y.L. Wang, W.M. Qiao, L.C. Ling, *J. Power Sources* 220 (2012) 342–347.
- [10] D. Song, H. Ikuta, T. Uchida, M. Wakihara, *Solid State Ionics* 117 (1999) 151–156.
- [11] A. Cao, A. Manthiram, *Phys. Chem. Chem. Phys.* 14 (2012) 6724–6728.
- [12] X.K. Huang, Q.S. Zhang, H.T. Chang, J.L. Gan, H.J. Yue, Y. Yang, *J. Electrochem. Soc.* 156 (2009) A162–A168.
- [13] K. Numata, C. Sakaki, S. Yamanaka, *Chem. Lett.* 26 (1997) 725–726.
- [14] G.M. Koenig, I. Belharouak, H. Deng, Y.K. Sun, K. Amine, *Chem. Mater.* 23 (2011) 1954–1963.
- [15] M. Tabuchi, A. Nakashima, H. Shigemura, K. Ado, H. Kobayashi, H. Sakaebi, H. Kageyama, T. Nakamura, M. Kohzaki, A. Hirano, R. Kanno, *J. Electrochem. Soc.* 149 (2002) A509–A524.
- [16] B. Ammundsen, J. Paulsen, *Adv. Mater.* 13 (2001) 943–956.
- [17] T.L. Zhao, S. Chen, L. Li, X.F. Zhang, R.J. Chen, I. Belharouak, F. Wu, K. Amine, *J. Power Sources* 228 (2013) 206–213.
- [18] M. Tabuchi, H. Shigemura, K. Ado, H. Kobayashi, H. Sakaebi, H. Kageyama, R. Kanno, *J. Power Sources* 97–98 (2001) 415–419.
- [19] M. Tabuchi, Y. Nabeshima, K. Ado, M. Shikano, H. Kageyama, K. Tatsumi, *J. Power Sources* 174 (2007) 554–559.
- [20] M. Tabuchi, Y. Nabeshima, T. Takeuchi, K. Tatsumi, J. Imaizumi, Y. Nitta, *J. Power Sources* 195 (2010) 834–844.
- [21] K. Karthikeyan, S. Amaresh, G.W. Lee, V. Aravindan, H. Kim, K.S. Kang, W.S. Kim, Y.S. Lee, *Electrochim. Acta* 68 (2012) 246–253.
- [22] M. Tabuchi, Y. Nabeshima, T. Takeuchi, H. Kageyama, K. Tatsumi, J. Akimoto, H. Shibuya, J. Imaizumi, *J. Power Sources* 196 (2011) 3611–3622.
- [23] M. Tabuchi, Y. Nabeshima, T. Takeuchi, H. Kageyama, J. Imaizumi, H. Shibuya, J. Akimoto, *J. Power Sources* 221 (2013) 427–434.
- [24] Z.H. Lu, J.R. Dahn, *J. Electrochem. Soc.* 149 (2002) A1454–A1459.
- [25] L.F. Jiao, M. Zhang, H.T. Yuan, M. Zhao, J. Guo, W. Wang, X.D. Zhou, Y.M. Wang, *J. Power Sources* 167 (2007) 178–184.
- [26] N.K. Karan, M. Balasubramanian, D.P. Abraham, M.M. Furczon, D.K. Pradhan, J.J. Saavedra-Arias, R. Thomas, R.S. Katiyar, *J. Power Sources* 187 (2009) 586–590.

- [27] Z.H. Lu, L.Y. Beaulieu, R.A. Donaberger, C.L. Thomas, J.R. Dahn, *J. Electrochem. Soc.* 149 (2002) A778–A791.
- [28] M.M. Thackeray, S.H. Kang, C.S. Johnson, J.T. Vaughan, R. Benedek, S.A. Hackney, *J. Mater. Chem.* 17 (2007) 3112–3125.
- [29] Z.H. Lu, J.R. Dahn, *J. Electrochem. Soc.* 149 (2002) A815–A822.
- [30] C.S. Johnson, N. Li, C. Lefief, J.T. Vaughan, M.M. Thackeray, *Chem. Mater.* 20 (2008) 6095–6106.
- [31] J.A. Dean, *Lange's Handbook of Chemistry*, fifteenth ed., McGraw-Hill, New York, 1998.
- [32] J. Kikkawa, T. Akita, M. Tabuchi, K. Tatsumi, M. Kohyama, *J. Electrochem. Soc.* 158 (2011) A760–A768.
- [33] L.B. Chen, K. Wang, X.H. Xie, J.Y. Xie, *J. Power Sources* 174 (2007) 538–543.
- [34] E.G. Shim, T.H. Nam, J.G. Kim, H.S. Kim, S.I. Moon, *J. Power Sources* 175 (2008) 533–539.